Editors' Suggestion

Ultrafast dynamics of photoexcited carriers in tellurium in the vicinity of Weyl nodes

Xiao Zhuo,[1] Qinsheng Wang,[2] Bin Cheng,[3,4,5] Delang Liang,[1,6] Haimen Mu,[3,4] Lin Li,[3,4,5] Zhengfei Wang,[3,4] Anlian Pan,[6] Changgan Zeng,[3,4,5] and Dong Sun[1,7,8,*]

[1]*International Center for Quantum Materials, School of Physics, Peking University, Beijing 100871, China*
[2]*Key Laboratory of Advanced Optoelectronic Quantum Architecture and Measurement (MOE), School of Physics, Beijing Institute of Technology, Beijing 100081, China*
[3]*International Center for Quantum Design of Functional Materials, Hefei National Laboratory for Physical Sciences at the Microscale, University of Science and Technology of China, Hefei, Anhui 230026, China*
[4]*Synergetic Innovation Center of Quantum Information and Quantum Physics, University of Science and Technology of China, Hefei, Anhui 230026, China*
[5]*Chinese Academy of Sciences Key Laboratory of Strongly Coupled Quantum Matter Physics, Department of Physics, University of Science and Technology of China, Hefei, Anhui 230026, China*
[6]*Key Laboratory for Micro-Nano Physics and Technology of Hunan Province, Hunan Institute of Optoelectronic Integration, College of Materials Science and Engineering, Hunan University, Changsha 410082, China*
[7]*Collaborative Innovation Center of Quantum Matter, Beijing 100871, China*
[8]*State Key Laboratory for Mesoscopic Physics and Frontiers Science Center for Nano-optoelectronics, School of Physics, Peking University, Beijing 100871, China*

(Received 15 May 2024; revised 27 June 2024; accepted 12 July 2024; published 24 July 2024)

Tellurium (Te) has recently attracted research interest for its outstanding electronic and optoelectronic properties and interesting topological physical related to topological Weyl cones in its band structure. To explore its high field transport and optoelectronic properties, the study of the ultrafast dynamics of photoexcited carriers plays a pivotal role. In this work, we study the ultrafast dynamics of photoexcited carriers in Te at the vicinity of Weyl nodes using transient reflection spectroscopy with 2-μm pump and 4-μm probe. We find that the relaxation process in a 100-nm Te flake is dominated by a 30-ps Auger recombination at high carrier density and a 200-ps multiphonon emission process at low carrier density. In contrast, the relaxation process in a 20-nm flake is ten times faster than the 100-nm flake due to the assistance of surface defects. The reflection modulation depth of the 20-nm sample is up to 60%, promising great potential for fast optical switch and optical modulator applications in the midinfrared region.

DOI: 10.1103/PhysRevB.110.014311

I. INTRODUCTION

Elemental tellurium (Te), which is traditionally regarded as a narrow-band-gap semiconductor [1,2], has recently been rediscovered as a reported Weyl semiconductor [3–5]. At the early stage, the research interests mainly originate from its high mobility [6,7], high photodetectivity [6,8], excellent air stability [7–9], and versatile tunable properties by conventional approaches such as electric gating [10]. Recent discovery of topological characteristics has made Te more attractive for high-performance electronic and optoelectronic devices [4,5,10,11]. From the perspective of functional high field electronic and optoelectronic devices applications, it is critical to study the ultrafast carrier dynamics of photoexcited carriers in Te [12,13]. This is because under high field, the carriers gain additional energy and become "hot" [12,14–16]. These hot carriers in the excited state govern the transport and photoelectric conversion and thus the performance of the devices. For example, in the context of optical modulators and optical switches, the modulation depth and operation speed are directly determined by the magnitude of transient modulation and carrier lifetime of photoexcited hot carriers [17–20]. In the context of the photodetector, the sensitivity and detection speed are determined by the separation of photoexcited electron/hole pairs and photoexcited carrier lifetime [21–23]. Thus, it is highly desired to study the photoexcited hot carrier dynamics of Te as the candidate materials for midinfrared optoelectronic devices.

Before this work, there have been several ultrafast studies on the Te flakes in the midinfrared region [24,25]. These studies claimed that radiative recombination is an important carrier relaxation channel in Te. However, the lifetime of the radiative recombination process is predicted to be longer than 10 ns from first principles density functional theory [26], which is much longer than the observed lifetime in previous experiments. On the other hand, the above studies were before the awareness of the topological properties of Te and no special attention was paid to the dynamics of photoexcited carriers in the vicinity of Weyl nodes. In this work, midinfrared pump-probe transient reflection spectroscopy is performed to study the dynamical evolution of photoexcited

*Contact author: sundong@pku.edu.cn

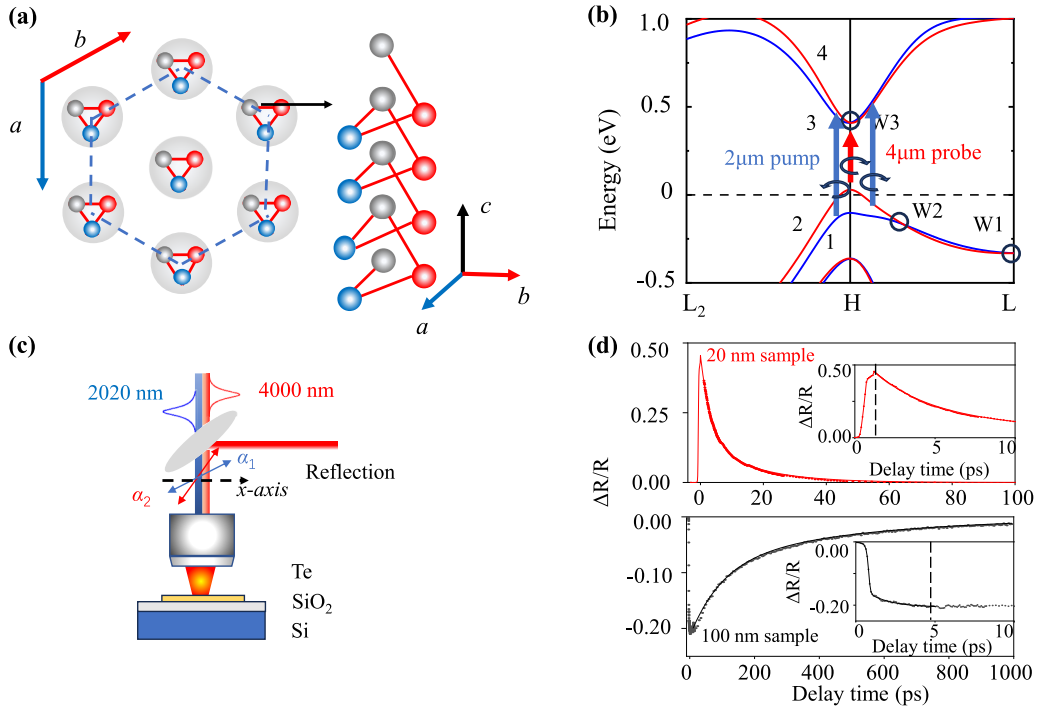

FIG. 1. Experimental scheme, lattice, and band structure of Te and typical transient reflection spectrum. (a) Lattice structure of Te. (b) Band structure of Te, W1, W2, and W3 marks three Weyl nodes near H point. Energy bands forming W1, W2, and W3 are marked by 1–4. The blue and red arrows represent the transitions of 2-μm pump and 4-μm probe photons, respectively. (c) Scheme of 2-μm pump and 4-μm probe ultrafast TR measurement setup. (d) Transient reflection spectrums of the 100-nm Te flake and the 20-nm Te flake at room temperature. The pump and probe polarizations are both parallel to crystallographic c axis and the pump fluences are both 80 μJ/cm^2. The results are fitted by biexponential decay function $\Delta R/R = A_1 e^{-t/\tau_1} + A_2 e^{-t/\tau_2}$. The inset figures show the TR signal near time zero.

carriers in the vicinity of the Weyl nodes in Te. We find that the dynamical response of Te flakes with different thickness is quite different due to different levels of surface defects. The relaxation process of photoexcited carriers in a 100-nm sample consists of a 30-ps Auger recombination process at initial high carrier density and a 200-ps multiphonon emission process. On the other hand, the relaxation channels in a 20-nm sample correspond to a 3-ps defect-assisted Auger recombination and a 10-ps cascade capture process. We also find that the magnitude of the modulation depth of the 20-nm Te flake is up to 60% with 120 μJ/cm^2 excitation energy, which is comparable to typical materials that are used in an optical switch such as gallium phosphide [27,28]. The high modulation depth and fast carrier relaxation time support that the thin Te flake can be a material candidate for a fast optical switch in the midinfrared region.

II. METHODS

Growth of film Te. Te flakes were grown by hydrothermal method following previous reports [6,7]. The thickness of the grown Te flakes ranged 20–120 nm. Te flakes were transferred onto 285-nm SiO_2/Si substrate through a drop-casting process for the transient reflection spectroscopy experiment.

Transient reflection spectroscopy. The origin 808-nm (1.53 eV) laser is generated by a 250-kHz Ti-sapphire regenerative amplifier (RegA). The 808-nm beam is used as the pump laser of an infrared optical parametric amplifier (OPA) to generate a 1315-nm signal and a 2020-nm idler. The wavelength of the signal and idler is determined by a spectrometer. Then the signal and 90% of the idler are used to pump a difference frequency generator (DFG) to generate 4 μm and used as probe of the transient reflection spectroscopy. Ten percent of the idler is used as pump of the transient reflection spectroscopy. The linear polarizations of pump and probe beams are rotated by their respective half wave plates. A 300-mm translation stage is used to adjust the delay time between the pump and probe. The combined lasers are focused by a 40× reflection objective onto the Te flake. The spot size of the probe laser is about 10 μm and the spot size of the pump is slightly larger. The reflection beam is filtered by a 2400-nm-long pass window and a spectrometer. An InSb detector is used to detect the reflection signal. A lock-in amplifier referenced to a mechanical chopper running at 443 Hz is used to read the transient reflection signal of the probe.

III. RESULTS

Te is a topological Weyl semiconductor with indirect band gap. The crystal structure of Te is shown in Fig. 1(a). The lattice structure of Te belongs to trigonal crystal lattice. It is formed by triple helix chains which are parallel to the crystallographic c axis. The inverse and mirror symmetries are both broken in Te. Past works have confirmed that bulk Te is a narrow-band-gap semiconductor with an indirect band gap ranging 0.28–0.38 eV near the H point in momentum space as shown in Fig. 1(b) [1,2,5,6]. The Weyl nodes of Te are located

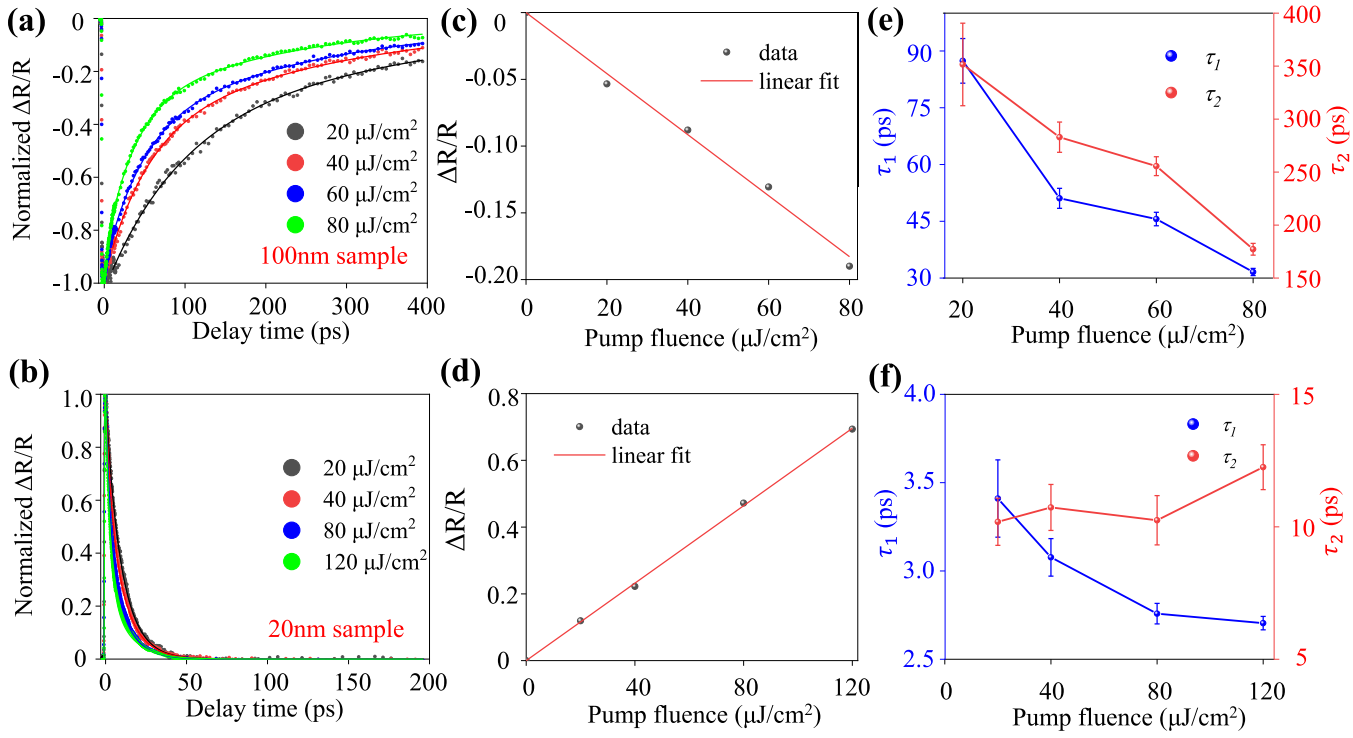

FIG. 2. Pump fluence dependence of transient reflection spectra. (a),(b) Transient reflection spectrums with 20-, 40-, 60-, 80$-\mu$J/cm^2 pump fluence of 100-nm Te flake and 20-nm Te flake, respectively. The results are fitted by biexponential decay function $\Delta R/R = A_1 e^{-t/\tau_1} + A_2 e^{-t/\tau_2}$. (c),(d) $\Delta R/R$|max as a function of pump fluence of 100-nm Te flake and 20-nm Te flake, respectively. The red lines are linear fit. (e),(f) Decay time constants τ_1, τ_2 with different pump fluence of 100-nm Te flake and 20-nm Te flake, respectively.

along the *H*-*L* direction as shown in Fig. 1(b). Weyl cones W1 and W2 are formed by the cross spin-splitting valence band 1 and band 2 while Weyl cone W3 is formed by the cross spin-splitting conduction band 3 and band 4. The selection rules determine that left circular polarized light (LCP) is preferable for transition from band 2 to band 3 while right circular polarized light (RCP) is preferable for the transition from band 1 to band 4 as revealed in previous work [10,11].

The photoexcited carrier dynamics of Te is studied by the ultrafast transient-reflection (TR) spectroscopy with schematic diagram shown in Fig. 1(c). In the measurement, the pump wavelength is set at 2 μm (0.62 eV) to excite the carriers near the *H* point in momentum space. The probe wavelength is set at 4 μm (0.31 eV) to study the dynamics near Weyl cone W3 at the *H* point of the conduction band. The pump and probe beams are either linear or circular polarized and the polarization direction can be rotated by either half or quarter wave plates. The time resolution of the transient measurement is limited by the 300-fs temporal convolution between the pump and probe pulses.

Figure 1(d) shows the typical transient reflection spectrum of a 20-nm Te flake and a 100-nm Te flake at room temperature. The penetration depth of Te is about 50 nm in the midinfrared region according to the literature [1,25]. According to the data shown in Fig. 1(d), both the pump and probe polarizations are linearly polarized along the *c* axis. The pump fluence is 80 μJ/cm^2 and the polarization direction of the pump and probe are both parallel to the crystallographic *c* axis. The transient reflection (TR) signals of the 20-nm and 100-nm flakes are very different. The TR signals of both flakes can be fitted by biexponential functions $\Delta R/R = A_1 e^{-t/\tau_1} + A_2 e^{-t/\tau_2}$. The decay rate of the 20-nm flake is obviously faster. The fast decay time constant τ_1 of the 20-nm flake is 2.75 ps while the slow decay time constant τ_2 is 10.3 ps. In contrast, the two decay time constants τ_1, τ_2 of the 100-nm flake are 31.6 and 177.7 ps, respectively, implying both decay processes are getting slower for thicker flakes. The signs of the TR signal of the two flakes are opposite: the reflection of the 100-nm flake decreases while the reflection of the 20-nm flake increases after the pump excitation and the TR signal of the 20-nm flake at time zero is about twice that of the 100-nm flake.

Next, we present a further pump fluence dependent measurement about the carrier relaxation dynamics of Te as shown in Fig. 2. The TR signals of 100-nm Te flake and the 20-nm flake with different pump fluences are shown in Figs. 2(a) and 2(b), respectively. The polarization direction of both pump and probe light are along the crystallographic *c* axis. As shown in Figs. 2(c) and 2(d) the magnitude of the TR signal at time zero can reach 67% and 19% for the 20-nm and 100-nm flake, respectively. The probe modulation depth $\Delta R/R$ is comparable to those typical materials used in an optical switch such as gallium phosphide [27]. The absolute reflectance along the *c* axis of the 100-nm flake and the 20-nm flake are 19% and 10%, respectively. We also note that the large modulation depth is possibly related to Weyl node W3 of Te. It has been reported that the optical transitions located at the position of Weyl points play the main role in the absorption process of

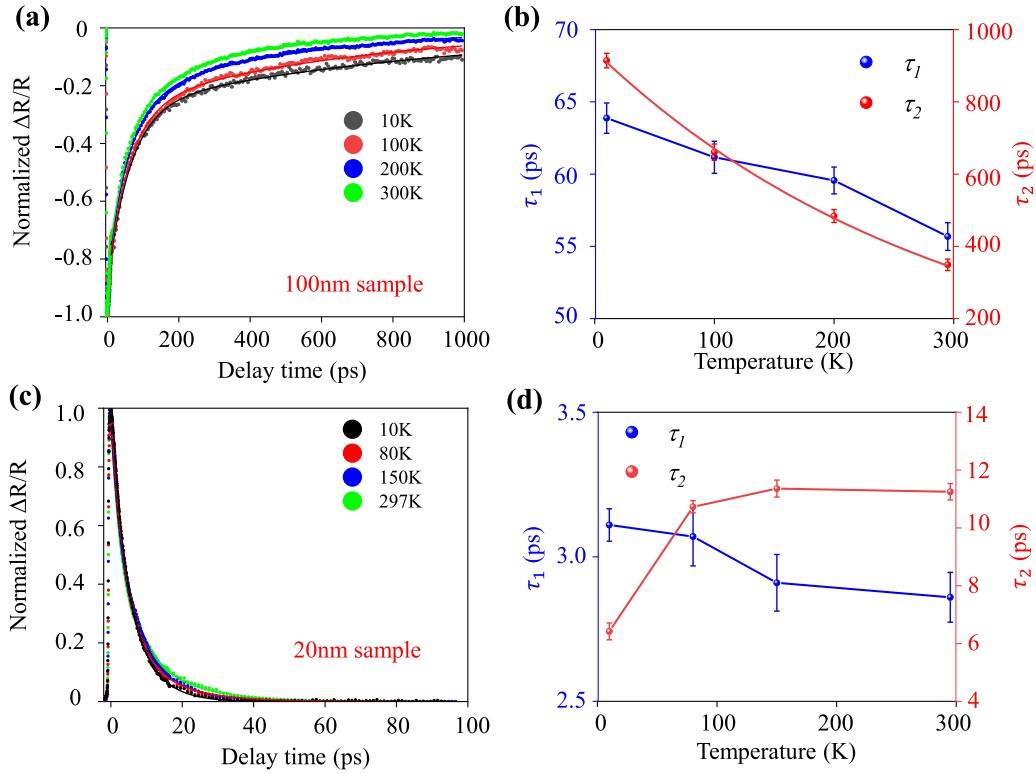

FIG. 3. Temperature dependence of TR dynamics. (a),(c) Normalized TR dyanmics (normalized with $\Delta R/R|\text{max}$) of the 100-nm (a) and the 20-nm (c) Te flakes at 10, 80, 150, and 297 K, respectively. The solid lines are biexponential fittings $\Delta R/R = A_1 e^{-t/\tau_1} + A_2 e^{-t/\tau_2}$. (b),(d) Fitted decay time constants τ_1, τ_2 as a function of temperature of the 100-nm (b) and the 20-nm (d) Te flakes, respectively.

Te [29]. The pump laser would lead to the occupancy of the Weyl cone at Weyl node W3 by photoexcited carriers. Thus, the reflection and the absorption of the 4-μm probe laser is highly modulated.

Figures 2(c) and 2(d) show the pump fluence dependence of the maximum TR peaks ($\Delta R/R|_{t=0}$) of the two flakes, which both depend linearly on the pump fluence. The linear dependence relation indicates that $\Delta R/R|_{t=0}$ has a linear dependence on photoexcited carrier density. Figures 2(e) and 2(f) show the biexponential fittings of the transient relaxation dynamics of TR. For the 100-nm flake, the fast decay time constant τ_1 decreases from 87 to 31 ps, while the slow decay time constant τ_2 decreases from 351 to 177 ps, when the pump fluence increases from 20 to 80 $\mu J/cm^2$. τ_1 of the 20-nm flake also decreases when pump fluence increases. However, the dependence of τ_2 on the pump fluence is not clear or very weak.

Figure 3 presents the temperature dependence of the TR signal of the 20- and 100-nm Te flakes. The polarizations of both the pump and probe are parallel to the c axis, and the pump fluence is 40 $\mu J/cm^2$. The temperature dependence of the relaxation processes of the 20- and 100-nm flakes are very different. According to the normalized TR spectra shown in Fig. 3(a), the decay of the 100-nm flake became slower at lower temperature. The biexponential fittings of the two decay time constants at different temperatures are shown in Fig. 3(b). When the temperature increases from 10 to 300 K, τ_1 decreases from 63.8 to 55.7 ps, while τ_2 decreases from 914 to 350 ps. The temperature dependence of τ_2 can be well fitted by an exponential function $\tau_2 = Be^{-\alpha T}$ with $B = 951$ ps and $\alpha = 0.0034\,\text{K}^{-1}$. Similar to that of the 100-nm flake, τ_1 of the 20-nm flake decreases when the temperature increases, while τ_2 shows no clear or very weak dependence on temperature, as shown in Fig. 3(d).

Now we turn to the interpretation of the fast and slow decay processes of the 20- and 100-nm Te flakes according to the pump fluence and temperature dependent measurement results. First, we can rule out the contribution from the radiative recombination process of photoexcited carriers. Te belongs to the indirect band semiconductor and the direct radiative recombination process is not efficient. Our photoluminescent measurements on the same flake shows very low emission which is consistent with the report in the literature [30]. Furthermore, the lifetime of the radiative recombination process is predicted to be longer than 10 ns in the literature [26], which is much longer than both τ_1 and τ_2 observed in our measurements. So we can determine that the contribution from the radiative recombination process is minor in TR relaxation of either the 20- or the 100-nm Te flake.

Next, we try to determine the nonradiative recombination dynamics. The nonradiative recombination can be an Auger process or a phonon-assisted process. A phonon-assisted recombination process can play the main role in the recombination process of topological semimetals [31–33]. This is because the energy and momentum conservation required for electron-phonon scattering is easily satisfied in gapless topological semimetals. However, Te is a semiconductor with a 0.36-eV band gap and the optical phonon energy of tellurium

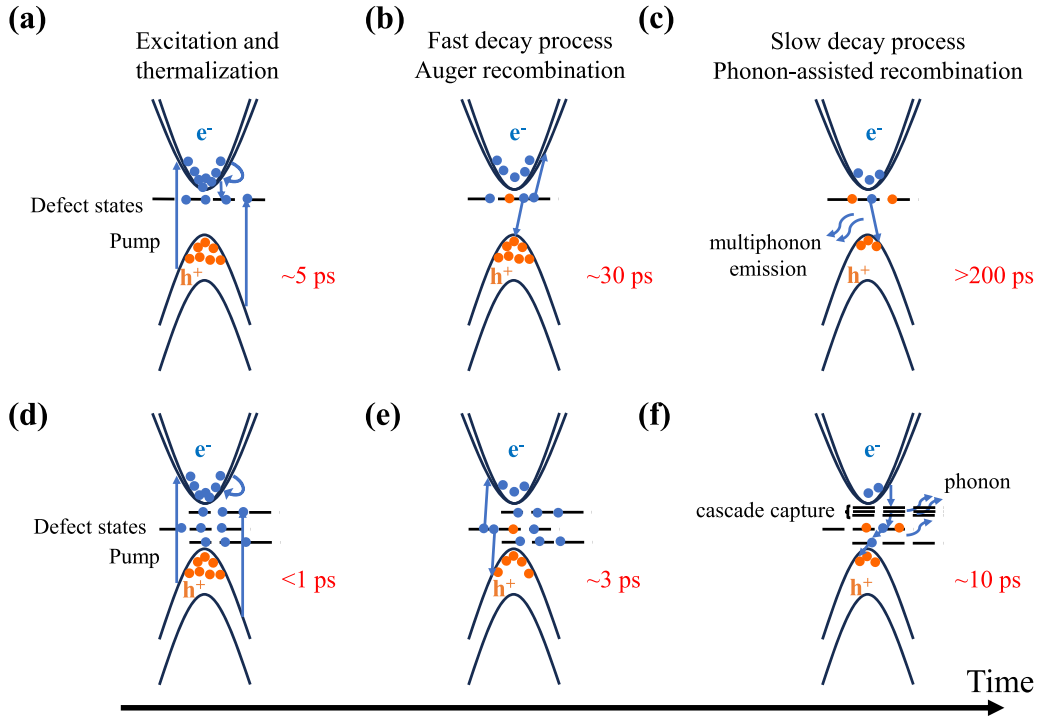

FIG. 4. Illustration of the ultrafast carrier dynamics of Te in three temporal regions; the upper and lower panels illustrate the dynamics of 100-nm flake and the 20-nm flake, respectively. (a) After photoexcitation, the electrons are excited to the defect states and the conduction band. The photoexcited carriers in the conduction band thermalize through a rapid carrier-carrier scattering process and reach a thermal equilibrium within hundreds of femtoseconds. Then, the carriers in the conduction band gradually decay to the defect states in 5 ps. (b) At high carrier density, the carriers in the defect states decay through Auger recombination. (c) At low carrier density, the carriers in the defect states decay through multiphonon emission. (d) After photoexcitation, the electrons are excited to the defect states and the conduction band; the photoexcited carriers in the conduction band thermalize through a rapid carrier-carrier scattering process and reach a thermal equilibrium within hundreds of femtoseconds. (e) At high carrier density, the carriers in the defect states decay through Auger recombination. (f) At low carrier density, the carriers in the defect states decay through cascade capture.

is 15 and 17 meV according to Raman spectra [34,35]. The phonon-assisted recombination process in Te should be a multiphonon process which should show clear temperature dependent behavior [36,37]. We note that the temperature dependence of τ_1 is weak for both 100- and 20-nm Te flakes, which indicates the fast decay process is not related to the phonon-assisted decay process. On the other hand, we note that τ_1 has strong pump fluence dependence for both thin and thick Te flakes: τ_1 decreases from 87 to 31 ps for the 100-nm flake and decreases from 3.4 to 2.7 ps for the 20-nm flake, when the pump fluence increases from 20 to 80 μJ/cm^2. The injection carrier density is 1.9×10^{20} and 9×10^{10} cm^{-3} for the 20- and 100-nm flake for pump fluence of 80 μJ/cm^2, respectively. The higher decay rate at higher carrier density is consistent with the characteristic of Auger recombination. The measured magnitude of the fast decay lifetime is also similar to that is observed in InAs with 0.36-eV band gap [38]. So, we can tentatively attribute the initial fast decay process τ_1 to Auger recombination. Here we note that τ_1 of the 20-nm flake is obviously much faster than the 100-nm flake. The contrast difference of τ_1 is unlikely relevant to band structure evolution with thickness, as the band structure stay almost the same when the thickness is over 10 nm, although previous work has demonstrated the band gap of Te has strong thickness dependence for very few layer flakes [6]. The faster Auger recombination process in the thinner flake is possibly assisted by the defect states [39].

In contrast to τ_1, τ_2 of the 100-nm flake shows strong dependence on the temperature. With the temperature increase from 10 to 297 K, τ_2 decreases from 914 to 349 ps. The exponential temperature dependence of τ_2 indicates that a decay process assisted by multiphonon emission [36,37] contributes to τ_2. In a multiphonon emission process, the energy and momentum of the carrier are transferred simultaneously to phonons. The phonon concentration is given by the Bose-Einstein distribution as $f(E) = 1/[\exp(E/k_BT) - 1] \approx \exp(-E/k_BT)$. Thus, the capture cross section is proportional to $\exp(-E/k_BT)$ and the carrier lifetime depends exponentially on the temperature [37,39]. The energy of optical phonons in Te are 15 and 17 meV. The long lifetime of the electron-phonon scattering process is possibly due to the relatively small optical-phonon energy. τ_2 of the 20-nm flake is not sensitive to the pump fluence and decreases at low temperature, which is quite different from that of the 100-nm flake. This indicates that the cascade capture process, which can be more effective at low temperature, possibly dominates the slow decay process in the 20-nm flake [37,40–43]. In a cascade capture process, electrons are first trapped on separated hydrogenlike excited states of the defect and decay from an excited state to another deeper one by

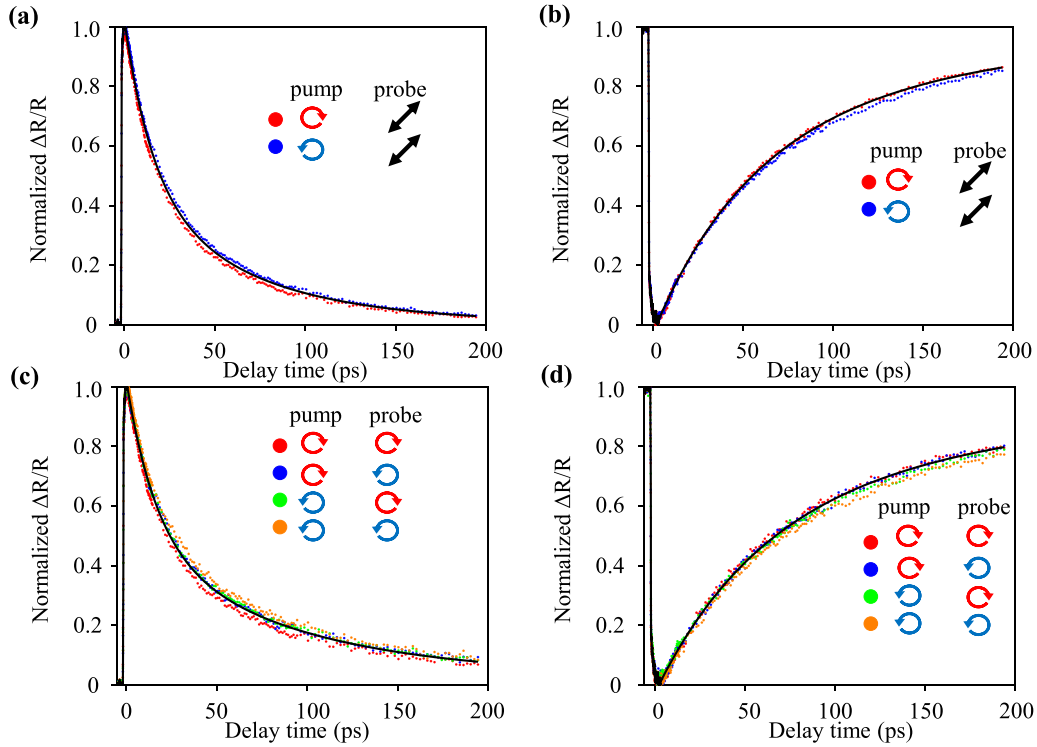

FIG. 5. Helicity dependence of transient reflection spectra. Transient reflection spectrums with circular polarized pump and linear polarized probe for a positive-TR flake (a) and a negative-TR flake (b), respectively. The pump polarizations are marked by the left and right symbols in the legend, respectively. The probe polarization is fixed at 45° to *c* axis. Transient reflection spectrums with circular polarization pump and probe for a positive-TR flake (c) and a negative-TR flake (d), respectively. The pump and probe polarizations are marked by the left and right symbols in the legend, respectively.

emitting a phonon. This mechanism is more operative at low temperature since at a higher temperature an electron cannot be trapped on an excited state, leading to a decreasing τ_2 with temperature.

We summarize the excitation and relaxation process of photoexcited carriers as shown in Fig. 4. The negative TR in the 100-nm flake indicates a photoinduced absorption. We notice a long rising time of about 5 ps in the 100-nm flake as shown in Fig. 1(d). The long rising time is much longer than the typical excitation and thermalization time of about hundreds of femtoseconds [12,44]. We suggest that there exist shallow defect states near the conduction band in the 100-nm flake as shown in Fig. 4(a). The 5-ps rising time contains the process that the photoexcited carriers decay to the defect states. The carriers in the defect state can be excited by the probe light and induce a photoinduced absorption which leads to the negative TR. Considering the 50-nm penetration depth of Te, there should be more defect states in the 20-nm flake due to the interface between Te and the substrate as shown in Fig. 4(b). Most of the carriers in the defect states cannot be excited by the probe light so that the photoinduced absorption is weak. The positive TR is due to the depletion of electrons in the valence band.

The differences of the relaxation process between the 100- and 20-nm flakes are also attributed to different densities of surface defects. In the case of the 100-nm flake, the excitation and thermalization of photoexcited carriers last for hundreds of femtoseconds. Then the carriers decay to the defects states in 5 ps. After that, the photoexcited carriers in the defect states start to decay mainly through Auger recombination. In about 30 ps, the carrier density becomes lower, and the electron-phonon scattering process gradually dominates the decay process. The photoexcited carriers decay to equilibrium through multiphonon emission in about 200 ps. For the 20-nm flake, the photoexcited carriers thermalized through a rapid carrier-carrier scattering process and reached a thermal equilibrium within hundreds of femtoseconds after pump excitation. Then the carriers decay mainly through defect-assisted Auger recombination in 3 ps at the initial high photoexcited carrier density. The timescale is shorter compared to thicker flakes because of a larger density of defect states in thinner flakes. When the carrier density becomes low after 3 ps, the carriers decay to equilibrium in about 10 ps mainly through cascade capture of the defect states. We also exclude the impact of the probe wavelength and the doping level by performing transient reflection spectra at a different probe wavelength and tuning the doping level with external gate as shown in Supplemental Materials S1 and S2 [45], which further prove that the difference in the reflectance change is attributed to the defect states.

At last, we also performed helicity dependent measurement to explore the chiral related dynamics. We first study the circular dichroism of pump excitation with circular polarized pump and linear polarized probe as shown in Figs. 5(a) and 5(b). However, no clear dependence on the pump helicity is observed in the TR dynamics. Although there are circular selection rules between spin polarized bands, the 2-μm pump can excite carriers from band 1 to band 4 for RCP light and

from band 2 to band 3 for LCP light. When polarization of the 2-μm pump switches from LCP to RCP light, it turns out the possibilities of the two transitions from band 2 to band 3 and the transition from band 1 to band 4 are similar, so that the absorption of LCP and RCP of pump light shows no difference in the circular polarization dependent measurement. We also study the helicity dependent dynamics with circular polarized pump and probe as shown in Figs. 5(c) and 5(d). There is still no obvious difference between TR with different pump and probe helicity. These results also support that the relaxation process is highly relevant to defect state so that the contribution of the selection rule cannot be clearly observed.

IV. CONCLUSION

In summary, we have performed ultrafast infrared transient reflection spectroscopy on Te flakes with different thickness. The dynamical response timescale as well as relaxation mechanism of photoexcited carriers in Te is significantly affected by the thickness due to the different impact of surface defect states. For thinner flakes with higher density of surface defect states, the relaxation of photoexcited carriers are mainly attributed to the defect-assisted Auger recombination process and cascade capture process. While for thicker flakes where the density of surface defects is low, the relaxation timescale is much longer and Auger recombination process and multiphonon emission process are the main relaxation mechanism. For a thinner 20-nm Te flake, the defect-assisted Auger recombination process is about 3 ps and the cascade capture process lasts for about 10 ps. The 20-nm Te flake has a high modulation depth of reflection up to 60% and a short relaxation time, which can have high potential in an optical switch and optical modulator in the midinfrared region. On the other hand, in a thicker 100-nm flake, a 30-ps Auger recombination process and a 200-ps multiphonon emission process contribute to the relaxation process. This experimental work studies the fundamental carrier dynamics of Te and provides basic device physics toward understanding the behavior of optoelectronic devices and high-field devices based on Te. The dynamical response of photoexcited carriers in Te can be highly tunable by thickness. Together with the ultrahigh mobility, the two-dimensional layered structure, and the excellent air stability, Te holds great potential for high performance electronic and optoelectronic device applications.

ACKNOWLEDGMENTS

This project has been supported by the National Key Research and Development Program of China (Grants No. 2020YFA0308800 and No. 2021YFA1400100), the National Natural Science Foundation of China (Grants No. 12034001, No. 62250065, No. 62325401, No. 62227822, and No. 12074036), the Open Fund of State Key Laboratory of Infrared Physics (Grant No. SITP-NLIST-ZD-2023–02).

The authors declare no competing interests.

[1] S. Tutihasi, G. G. Roberts, R. C. Keezer, and R. E. Drews, Optical properties of tellurium in the fundamental absorption region, Phys. Rev. **177**, 1143 (1969).

[2] V. B. Anzin, M. I. Eremets, Y. V. Kosichkin, A. I. Nadezhdinskii, and A. M. Shirokov, Measurement of the energy gap in tellurium under pressure, Phys. Status Solidi **42**, 385 (1977).

[3] J. Chen, T. Zhang, J. Wang, L. Xu, Z. Lin, J. Liu, C. Wang, N. Zhang, S. P. Lau, W. Zhang, M. Chhowalla, and Y. Chai, Topological phase change transistors based on tellurium Weyl semiconductor, Sci Adv. **8**, eabn3837 (2022).

[4] G. Qiu, C. Niu, Y. Wang, M. Si, Z. Zhang, W. Wu, and P. D. Ye, Quantum Hall effect of Weyl fermions in n-type semiconducting tellurene, Nat. Nanotechnol. **15**, 585 (2020).

[5] N. Zhang, G. Zhao, L. Li, P. Wang, L. Xie, B. Cheng, H. Li, Z. Lin, C. Xi, J. Ke, M. Yang, J. He, Z. Sun, Z. Wang, Z. Zhang, and C. Zeng, Magnetotransport signatures of Weyl physics and discrete scale invariance in the elemental semiconductor tellurium, Proc. Natl. Acad. Sci. USA **117**, 11337 (2020).

[6] M. Amani, C. Tan, G. Zhang, C. Zhao, J. Bullock, X. Song, H. Kim, V. R. Shrestha, Y. Gao, K. B. Crozier, M. Scott, and A. Javey, Solution-synthesized high-mobility tellurium nanoflakes for short-wave infrared photodetectors, ACS Nano **12**, 7253 (2018).

[7] Y. Wang, G. Qiu, R. Wang, S. Huang, Q. Wang, Y. Liu, Y. Du, W. A. Goddard, M. J. Kim, X. Xu, P. D. Ye, and W. Wu, Field-effect transistors made from solution-grown two-dimensional tellurene, Nat. Electron. **1**, 228 (2018).

[8] L. Tong, X. Huang, P. Wang, L. Ye, M. Peng, L. An, Q. Sun, Y. Zhang, G. Yang, Z. Li, F. Zhong, F. Wang, Y. Wang, M. Motlag, W. Wu, G. J. Cheng, and W. Hu, Stable mid-infrared polarization imaging based on quasi-2D tellurium at room temperature, Nat. Commun. **11**, 2308 (2020).

[9] W. Wu, G. Qiu, Y. Wang, R. Wang, and P. Ye, Tellurene: Its physical properties, scalable nanomanufacturing, and device applications, Chem. Soc. Rev. **47**, 7203 (2018).

[10] J. Ma, B. Cheng, L. Li, Z. Fan, H. Mu, J. Lai, X. Song, D. Yang, J. Cheng, Z. Wang, C. Zeng, and D. Sun, Unveiling Weyl-related optical responses in semiconducting tellurium by mid-infrared circular photogalvanic effect, Nat. Commun. **13**, 5425 (2022).

[11] G. Gatti, D. Gosálbez-Martínez, S. S. Tsirkin, M. Fanciulli, M. Puppin, S. Polishchuk, S. Moser, L. Testa, E. Martino, S. Roth, P. Bugnon, L. Moreschini, A. Bostwick, C. Jozwiak, E. Rotenberg, G. Di Santo, L. Petaccia, I. Vobornik, J. Fujii, J. Wong *et al.*, Radial spin texture of the weyl fermions in chiral tellurium, Phys. Rev. Lett. **125**, 216402 (2020).

[12] D. Sun, Z.-K. Wu, C. Divin, X. Li, C. Berger, W. A. de Heer, P. N. First, and T. B. Norris, Ultrafast relaxation of excited dirac fermions in epitaxial graphene using optical differential transmission spectroscopy, Phys. Rev. Lett. **101**, 157402 (2008).

[13] F. H. L. Koppens, T. Mueller, P. Avouris, A. C. Ferrari, M. S. Vitiello, and M. Polini, Photodetectors based on graphene, other two-dimensional materials and hybrid systems, Nat. Nanotechnol. **9**, 780 (2014).

[14] S. Ge, C. Li, Z. Zhang, C. Zhang, Y. Zhang, J. Qiu, Q. Wang, J. Liu, S. Jia, J. Feng, and D. Sun, Dynamical evolution of anisotropic response in black phosphorus under ultrafast photoexcitation, Nano Lett. **15**, 4650 (2015).

[15] N. M. Gabor, J. C. W. Song, Q. Ma, N. L. Nair, T. Taychatanapat, K. Watanabe, T. Taniguchi, L. S. Levitov, and P. Jarillo-Herrero, Hot carrier–assisted intrinsic photoresponse in graphene, Science **334**, 648 (2011).

[16] X. Zhuo, J. Lai, P. Yu, Z. Yu, J. Ma, W. Lu, M. Liu, Z. Liu, and D. Sun, Dynamical evolution of anisotropic response of type-II Weyl semimetal $TaIrTe_4$ under ultrafast photoexcitation, Light: Sci. Appl. **10**, 101 (2021).

[17] Z. Chai, X. Hu, F. Wang, X. Niu, J. Xie, and Q. Gong, Ultrafast all-optical switching, Adv. Opt. Mater. **5**, 1600665 (2017).

[18] M. Hochberg, T. Baehr-Jones, G. Wang, M. Shearn, K. Harvard, J. Luo, B. Chen, Z. Shi, R. Lawson, P. Sullivan, A. K. Y. Jen, L. Dalton, and A. Scherer, Terahertz all-optical modulation in a silicon–polymer hybrid system, Nat. Mater. **5**, 703 (2006).

[19] W. Li, B. Chen, C. Meng, W. Fang, Y. Xiao, X. Li, Z. Hu, Y. Xu, L. Tong, H. Wang, W. Liu, J. Bao, and Y. R. Shen, Ultrafast all-optical graphene modulator, Nano Lett. **14**, 955 (2014).

[20] K. Nozaki, T. Tanabe, A. Shinya, S. Matsuo, T. Sato, H. Taniyama, and M. Notomi, Sub-femtojoule all-optical switching using a photonic-crystal nanocavity, Nat. Photonics **4**, 477 (2010).

[21] M. C. Lemme, F. H. L. Koppens, A. L. Falk, M. S. Rudner, H. Park, L. S. Levitov, and C. M. Marcus, Gate-activated photoresponse in a graphene p–n junction, Nano Lett. **11**, 4134 (2011).

[22] Q. Wang, C.-Z. Li, S. Ge, J.-G. Li, W. Lu, J. Lai, X. Liu, J. Ma, D.-P. Yu, Z.-M. Liao, and D. Sun, Ultrafast broadband photodetectors based on three-dimensional dirac semimetal Cd_3As_2, Nano Lett. **17**, 834 (2017).

[23] D. Sun, G. Aivazian, A. M. Jones, J. S. Ross, W. Yao, D. Cobden, and X. Xu, Ultrafast hot-carrier-dominated photocurrent in graphene, Nat. Nanotechnol. **7**, 114 (2012).

[24] V. Iyer, M. Segovia, Y. Wang, W. Wu, P. Ye, and X. Xu, Infrared ultrafast spectroscopy of solution-grown thin film tellurium, Phys. Rev. B **100**, 075436 (2019).

[25] G. Jnawali, Y. Xiang, S. M. Linser, I. A. Shojaei, R. Wang, G. Qiu, C. Lian, B. M. Wong, W. Wu, P. D. Ye, Y. Leng, H. E. Jackson, and L. M. Smith, Ultrafast photoinduced band splitting and carrier dynamics in chiral tellurium nanosheets, Nat. Commun. **11**, 3991 (2020).

[26] J. Hader, S. C. Liebscher, J. V. Moloney, and S. W. Koch, Intrinsic carrier losses in tellurium due to radiative and Auger recombinations, Appl. Phys. Lett. **121**, 192103 (2022).

[27] G. Grinblat, M. P. Nielsen, P. Dichtl, Y. Li, R. F. Oulton, and S. A. Maier, Ultrafast sub–30-fs all-optical switching based on gallium phosphide, Sci Adv. **5**, eaaw3262 (2019).

[28] G. Grinblat, H. Zhang, M. P. Nielsen, L. Krivitsky, R. Berté, Y. Li, B. Tilmann, E. Cortés, R. F. Oulton, A. I. Kuznetsov, and S. A. Maier, Efficient ultrafast all-optical modulation in a nonlinear crystalline gallium phosphide nanodisk at the anapole excitation, Sci Adv. **6**, eabb3123 (2020).

[29] Q. Fu, X. Cong, X. Xu, S. Zhu, X. Zhao, S. Liu, B. Yao, M. Xu, Y. Deng, C. Zhu, X. Wang, L. Kang, Q. Zeng, M.-L. Lin, X. Wang, B. Tang, J. Yang, Z. Dong, F. Liu, Q. Xiong *et al.*, Berry curvature dipole induced giant mid-infrared second-harmonic generation in 2D weyl semiconductor, Adv. Mater. **35**, 2306330 (2023).

[30] D. Choi and K. S. Midwavelength Jeong, Infrared photoluminescence and lasing of tellurium elemental solid and microcrystals, J. Phys. Chem. Lett. **10**, 4303 (2019).

[31] L. Cheng, F. C. Fei, H. Hu, Y. M. Dai, F. Q. Song, and J. Qi, Ultrafast carrier and lattice dynamics in the Dirac semimetal NTe_2, Phys. Rev. B **106**, 104308 (2022).

[32] Y. M. Dai, J. Bowlan, H. Li, H. Miao, S. F. Wu, W. D. Kong, P. Richard, Y. G. Shi, S. A. Trugman, J. X. Zhu, H. Ding, A. J. Taylor, D. A. Yarotski, and R. P. Prasankumar, Ultrafast carrier dynamics in the large-magnetoresistance material WTe_2, Phys. Rev. B **92**, 161104(R) (2015).

[33] Z. Wei, S. Zhang, Y. Su, L. Cheng, H. Zhou, Z. Jiang, H. Weng, and J. Qi, Extremely low-energy collective modes in a quasi-one-dimensional topological system, Sci. China Phys., Mech. Astron. **65**, 257012 (2022).

[34] Y. Du, G. Qiu, Y. Wang, M. Si, X. Xu, W. Wu, and P. D. Ye, One-dimensional van der Waals material tellurium: Raman spectroscopy under strain and magneto-transport, Nano Lett. **17**, 3965 (2017).

[35] J.-K. Qin, P.-Y. Liao, M. Si, S. Gao, G. Qiu, J. Jian, Q. Wang, S.-Q. Zhang, S. Huang, A. Charnas, Y. Wang, M. J. Kim, W. Wu, X. Xu, H.-Y. Wang, L. Yang, Y. Khin Yap, and P. D. Raman Ye, response and transport properties of tellurium atomic chains encapsulated in nanotubes, Nat. Electron. **3**, 141 (2020).

[36] A. Alkauskas, Q. Yan, and C. G. Van de Walle, First-principles theory of nonradiative carrier capture via multiphonon emission, Phys. Rev. B **90**, 075202 (2014).

[37] C. H. Henry and D. V. Lang, Nonradiative capture and recombination by multiphonon emission in GaAs and GaP, Phys. Rev. B **15**, 989 (1977).

[38] K. L. Vodopyanov, H. Graener, C. C. Phillips, and T. J. Tate, Picosecond carrier dynamics and studies of Auger recombination processes in indium arsenide at room temperature, Phys. Rev. B **46**, 13194 (1992).

[39] H. Wang, C. Zhang, and F. Rana, Ultrafast dynamics of defect-assisted electron–hole recombination in monolayer MoS_2, Nano Lett. **15**, 339 (2015).

[40] E. E. Orlova, R. W. Kelsall, N. Deßmann, S. G. Pavlov, H.-W. Hübers, R. K. Zhukavin, and V. N. Shastin, Cascade capture of charge carriers in highly doped semiconductors, J. Appl. Phys. **124**, 085704 (2018).

[41] D. R. Hamann and A. L. McWhorter, Cascade capture of electrons by ionized impurities, Phys. Rev. **134**, A250 (1964).

[42] M. Lax, Cascade capture of electrons in solids, Phys. Rev. **119**, 1502 (1960).

[43] B. K. Ridley, *Quantum Processes in Semiconductors*, 5th ed. (Oxford University Press, Oxford, 2013).

[44] C. Jin, E. Y. Ma, O. Karni, E. C. Regan, F. Wang, and T. F. Heinz, Ultrafast dynamics in van der Waals heterostructures, Nat. Nanotechnol. **13**, 994 (2018).

[45] See Supplemental Material at http://link.aps.org/supplemental/10.1103/PhysRevB.110.014311 for probe-wavelength and gate-voltage dependent transient reflection spectra.